

High-performance fiber reinforced concrete as a repairing material to normal concrete structures: Experiments, numerical simulations and a machine learning-based prediction model

Pengcheng Jiao^{a,*}, Manish Roy^b, Kaveh Barri^c, Ronghua Zhu^a, Indrajit Ray^d, Amir H. Alavi^{c,*}

^a Ocean College, Zhejiang University, Zhoushan 316021, Zhejiang, China

^b Department of Civil and Environmental Engineering, University of Connecticut, Storrs, CT 06269, USA

^c Department of Civil and Environmental Engineering, University of Pittsburgh, Pittsburgh, PA 15260, USA

^d Department of Civil and Environmental Engineering, University of the West Indies, St Augustine, Trinidad and Tobago

HIGHLIGHTS

- High-performance fiber reinforced concrete (HPFRC) is reported as repairing material to normal concrete (NC).
- HPFRC and NC samples are manufactured and experimentally calibrated.
- HPFRC-NC debonding test is conducted under direct shear load.
- A machine learning model is developed to predicted the shear debonding behavior of HPFRC-NC.

ARTICLE INFO

Article history:

Received 11 March 2019

Received in revised form 19 June 2019

Accepted 26 July 2019

Keywords:

High-performance fiber reinforced concrete (HPFRC)

Normal concrete (NC)

Debonding behavior

Machine learning

Prediction model

Direct shear test

ABSTRACT

High-performance fiber reinforced concrete (HPFRC) has been reported as a repairing material to normal concrete (NC) structures due to its predominant mechanical performance. Here, we investigate the debonding behavior between HPFRC and NC subjected to direct shear loading. HPFRC specimens are fabricated and experimentally calibrated to determine the compressive and bending (i.e., flexural) strengths. HPFRC-NC samples are fabricated using two bonding strategies, i.e., mechanical surface treatments with and without chemical agent. Direct shear loading is applied to test the HPFRC-NC debonding behavior. A finite element (FE) model is developed to predict the direct shear debonding response. The FE model is validated by the experimental observations and then used to characterize the debonding behavior with various geometric and material parameters, as well as bonding interface treatments. Subsequently, a robust machine learning model is developed to formulate the shear debonding strength of HPFRC-NC with those influencing parameters. Design examples are presented to illustrate the efficiency of the proposed machine learning model in describing the debonding response of HPFRC-NC. A sensitivity analysis is further conducted to investigate the contribution of the chosen predictors to the debonding behavior of HPFRC-NC. The reported HPFRC and machine learning-based prediction model provide powerful tools to address repairing issues in various existing normal concrete structures.

© 2019 Elsevier Ltd. All rights reserved.

1. Introduction

High-performance fiber reinforced concrete (HPFRC) is a special class of fiber reinforced concrete (FRC), which shows promising deflection-hardening behavior under deformation. The flexural strength is similar to that of high-performance fiber reinforced cementitious composites (HPFRCC) and engineered cementitious composites (ECC), which is much higher than high-performance

concrete (HPC). The compressive strength of HPFRC is higher than that of HPFRCC, ECC, and HPC, but is lower than ultra-high-performance concrete (UHPC) [38]. By virtue of its improved mechanical behaviors and enhanced bond properties [38,36], HPFRC has the potential to be used as an effective repairing material to existing concrete structures. For example, the loading capacity and the durability of concrete members are significantly impacted by corrosion of steel rebar due to chloride and moisture penetrations through cracks. Those corroded rebars lead to the degradations in concrete members and therefore, aggravate the risk of structural failure. To demonstrate the advanced

* Corresponding authors.

E-mail addresses: pjiao@zju.edu.cn (P. Jiao), alavi@pitt.edu (A.H. Alavi).

performance of HPFRC in civil infrastructures, research efforts have been dedicated to understanding: a) mechanical behavior of the material under different loading conditions, and b) bonding/debonding response between HPFRC (as a repairing agent) and existing, damaged normal concrete.

Studies have been conducted to characterize the mechanical response of HPFRC subjected to different loading conditions, e.g., pure axial loading [19], high strain rates [46], blast loading [6], and seismic loading [28]. Pourbaba et al. [33] experimentally investigated the effect of aging on compressive strength of HPFRC columns. Nonlinear finite element analysis was carried out to reveal the flexural behavior of HPFRC beams by Yoo et al. [51]. Zhou and Uchida [54] examined the effect of fibers on the post-cracking response of HPFRC, and quantitatively evaluated the impacts of fiber orientation and distribution. Xia et al. [49] presented a size-independent constitutive model to study crack propagation of HPFRC for sectional flexural analysis. Many studies have also been carried out to investigate the mechanical response of concrete structures that use HPFRC as a repairing material, e.g., flexural behavior [40,5], tensile properties [39], and seismic behavior [20]. Tayeh et al. [45] experimentally characterized the bonding behavior between existing concrete substrates and HPFRC repair materials. Li et al. [23] studied the mechanical behavior of damaged reinforced concrete (RC) repaired by HPFRC and proposed a repairing technique for RC columns damaged in earthquake. Other than characterizing the mechanical properties of HPFRC as a repairing material, it is also of interest to accurately predict the repairing behavior of HPFRC under different loading conditions.

Precisely predicting the mechanical performance of HPFRC-repaired concrete structures is required in different applications such as many design practices and scheduling operations in civil constructions. To obtain the mechanical behavior, i.e., compressive strength or debonding limit, studies have been reported on prediction models developed using experimental, numerical or theoretical approaches [10]. Radtke et al. [34] proposed a computational model to describe the failure processes of HPFRC, which led to a discrete approach to investigate the effect of fiber distribution on the behavior of the material. A dynamic mesoscale model was developed to quantify the energy dissipation of HPFRC under rapid loading [13]. The authors took into account three constituent components, namely reinforcement fibers, cementitious matrix, and fiber–matrix interfaces. Yoo et al. [52] studied the effect of micro-scale steel fibers on the interfacial bonding behavior between HPFRC and normal concrete. Lampropoulos et al. (2015) developed a finite element (FE) model based on the tensile and compressive strength experiments between UHPFRC and existing reinforced concrete (RC). Traditional regression techniques have been extensively used to develop prediction models for mechanical properties of various types of concrete. However, traditional regression requires to define the functional representation of the model in advance, which, arguably, is not an optimal solution for mechanical parameters that involve high nonlinearities [2]. In recent years, machine learning (ML) approaches, a subdivision of artificial intelligence inspired by biological learning processes, have been extensively applied as a prominent empirical regression tool to address issues in civil engineering design [22,3]. ML methods can particularly learn the underlying behavior of a system from sets of training data without clarifying the relationship between those data. Therefore, an ML-based prediction model does not need to have predefined functional representation of the model. Powerful ML techniques such as genetic programming (GP), artificial neural networks (ANN), support vector machines (SVM), and decision model tree have been successfully deployed to solve various civil engineering problem, such as mechanical characterization of high-performance concrete [3,27,9,43,44]. One of the main advantages of GP and its branches over other ML methods (e.g., ANN, SVM)

is that they can generate a transparent and structured representation of the system being studied.

In this study, we first experimentally characterize the effect of granular mixture on the mechanical behavior of the HPFRC-repaired normal concrete samples (i.e., HPFRC-NC). Based on the experimental results, a FE model is developed to foresee the debonding response of HPFRC-NC. In addition, we propose a novel strategy for the calibration of the ML algorithm. To this aim, the FE simulation results are thoroughly validated by the experimental observations. The calibrated FE models are then used to characterize the debonding behavior with respect to various geometric and material parameters, as well as the bonding interface treatments of HPFRC-NC. The developed database is utilized to train and establish a ML prediction model for the shear debonding strength of HPFRC-NC. The advantage of this strategy is that it eliminates the necessity of performing costly and time-consuming experiments that are typically required to create large database for calibrating ML models. Additionally, it provides a useful tool to investigate the effect of parameters on the debonding response between HPFRC and NC, which might not be easily plausible via laboratory testing.

The rest of the paper is organized as: Section 2 presents the HPFRC-NC debonding tests. The HPFRC specimens are first fabricated and calibrated to determine the mechanical properties. Debonding tests are then designed and carried out under direct shear loading. Section 3 proposes the numerical simulations of the debonding behavior. A concrete damage plasticity (CDP) model is developed in Abaqus, and the finite element (FE) predictions are validated by the experimental results. Section 4 develops an ML prediction model to formulate the shear debonding strength with the mixture proportions. Section 5 summarizes the main findings in this study. In Appendix, raw data of HPFRC-NC are provided.

2. HPFRC-NC shear debonding tests

2.1. Fabrication and experimental calibration of HPFRC

Fig. 1 presents the fabrication process of HPFRC. Fig. 1(a) shows the components of HPFRC, including portland cement, sand, steel

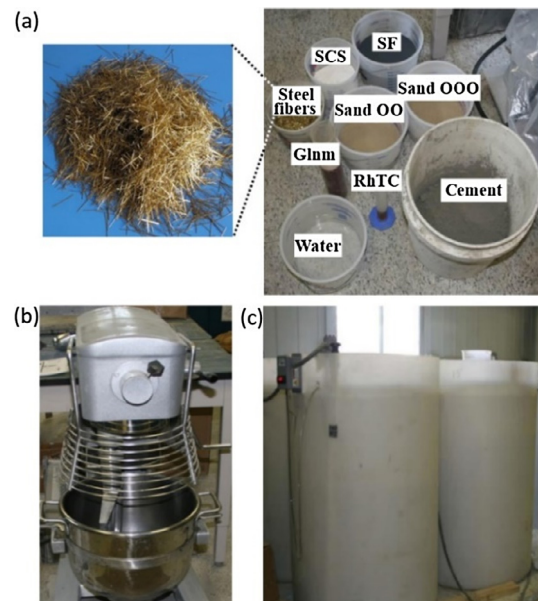


Fig. 1. (a) Components of HPFRC. (b) Constant speed mixer. (c) Temperature-controlled double-walled tanks.

fibers, Sil-co-Sil 90 (SCS), silica fume (SF), Glenium 7500 (Glnm), RheoTEC (RhTC), and water. In particular, type I portland cement conforming to ASTM C150 (i.e., Standard Specification for Portland Cement) was deployed with two types of fine natural sands (i.e., Sand OO and Sand OOO). Straight-drawn discontinuous steel fibers (OL 13/0.20) were used to increase the post-cracking ductility of HPFRC, as detailed in Fig. 1(a). SCS, containing crystalline silica (mineral quartz), was added as the third constituent in the fine aggregate category, while no coarse aggregate was used. Densified SF (i.e., Rheomac SF 100) was added as the mineral admixture, and high range water reducing admixture (i.e., Glnm) and workability retaining admixture (i.e., RhTC) were added as the chemical admixtures. To prevent HPFRC from overheating during mixing, cold and potable water ($\sim 10^\circ\text{C}$) was used, and the mixing time was more than that of the conventional concrete. See Appendix A for detailed material properties of the components in HPFRC.

Fig. 1(b) shows the 3-speed mixer with the capacity of 28.4 L used to mix HPFRC under the constant speed of 91 rpm. The mixing process can be summarized as: a. All the constituent materials were first weighed. b. Three different types of fine aggregates (i.e., Sand OO, Sand OOO, and Sil-co-sil 90) and silica fume were added to the bowl and mixed for 3 mins. c. Portland cement was added to the bowl and mixed for 3 mins. d. Water was added to the dry mix over a course of 30 s and the mixing was continued for 3 mins. e. Glnm and RhTC were then added and the mixing was continued until the mix turned to a thick paste. This process typically took 2 mins. f. Steel fibers were added to the paste and the mixer machine was continued to run (for about 2 mins) till the fibers were properly dispersed in the matrix. The prepared HPFRC was then poured into the molds. After 24 h of casting, the specimens were demolded and placed under water in a custom designed temperature controlled double-walled tank at 55°C until 1 day before testing. The mixing procedure and the curing conditions have been explained in detail in Roy [37] and Roy et al. [38]. Fig. 1(c) displays the temperature-controlled double-walled tanks.

To investigate the mechanical response of HPFRC, two types of mechanical tests were carried out, viz., compression and 3-point bending tests (as shown in Fig. 2). Fig. 2(a) presents the compression test. HPFRC cylinders were poured in the plastic cylindrical molds, which were then loaded using a 1000 KN MTS machine to measure the compressive stiffness. Displacement-control loading procedures were designed with a constant rate of 0.05 mm/s. Fig. 2(b) displays the 3-point bending test. The HPFRC beams were made in steel prismatic molds and the same MTS machine was



Fig. 2. (a) HPFRC specimens and the experimental setup for compressive stiffness test. (b) HPFRC specimens and the experimental setup for bending stiffness test.

Table 1

The geometric properties and loading conditions of the HPFRC specimens in the compression and bending tests.

	Parameter	Value
Compression test	Diameter (mm)	76
	Height (mm)	152
	Loading speed (mm/s)	0.05
Bending test	Width (mm)	76
	Height (mm)	76
	Length (mm)	285
	Span bt. supports (mm)	241
	Loading speed (mm/s)	0.015

used for the 3-point bending experiments. The specimens were loaded with the constant displacement rate of 0.015 mm/s [37]. The geometric properties and loading conditions of the HPFRC samples in the compression and bending tests are summarized in Table 1.

Fig. 3 displays the failure of the concrete samples in the compression and bending tests. Due to the incorporation of steel fibers in HPFRC, the broken configuration of cylinders in the compression test was approximately in the loading direction rather than $\sim 45^\circ$ from the principal plane, as shown in Fig. 3(a). Similar findings were obtained from the 3-point bending test for the bending stiffness, as presented in Fig. 3(b). Fig. 4 presents the mechanical performance of HPFRC calibrated in the experiments. Fig. 4(a) exhibits the compressive stiffness of the high-performance concrete, which first exhibits a linearly increasing force–displacement relationship with the spring constant K_{inc} . A sharp dropping of debonding resistance is obtained after the concrete reaches the maximum axial force F_{max} . Shortly after the significant dropping, HPFRC retains the compression resistance with the spring constant K_{dec} , which indicates the effectiveness of HPFRC's repairing performance as compared to high strength concrete without fiber, which shows a brittle failure with a sharp decline of the force in the softening regime. On the contrary, the bending stiffness in Fig. 4(b) shows a bi-linearly increasing force–displacement curve with the stiffnesses K_{inc1} and K_{inc2} indicating the deflection hardening behavior under flexure. However, it does not experience the critical dropping region; instead, the force decreases almost linearly after the maximum force F_{max} is reached. Table 2 summarizes the mechanical properties of HPFRC determined using experimental calibration.

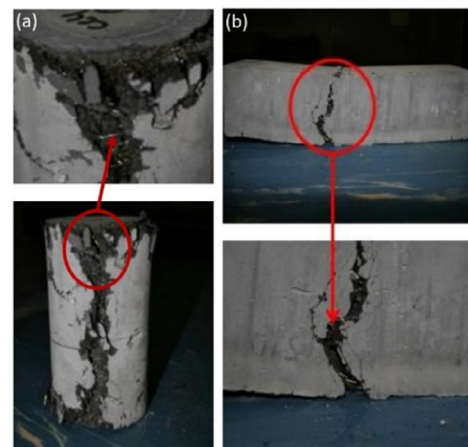


Fig. 3. Failure configurations of the HPFRC samples in (a) compression test and (b) bending test.

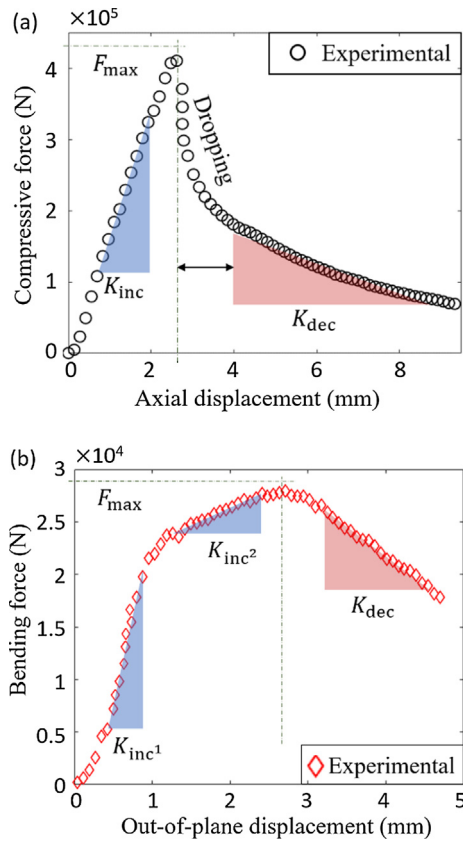


Fig. 4. Axial force-displacement responses of HPFRC subjected to (a) compression and (b) 3-point bending experiments.

Table 2
Material properties of HPFRC.

Density (kg/m^3)	2450
Young's Modulus (MPa)	49,467

2.2. HPFRC-NC shear debonding test

2.2.1. Design of debonding test

Butterfly-shaped specimens were used to test the debonding behavior between HPFRC and NC, as shown in Fig. 5. The bonding area was designed in the middle of the interface between the wings. Fig. 5(a) illustrates a bi-layered HPFRC-NC sample under shear force in the 3D perspective, and Fig. 5(b) and (c) indicate

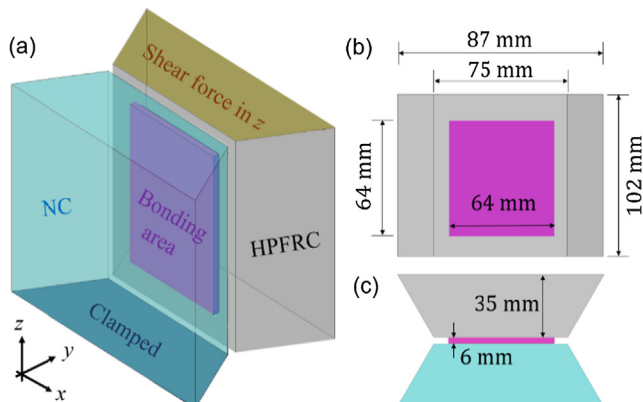


Fig. 5. (a) Illustration of the designed butterfly-shaped HPFRC-NC sample for direct shear debonding test in (a) 3D perspective, (b) side view, and (c) top view.

the geometries of the bonded sample in the side view and top view, respectively.

Fig. 6(a) shows the manufacturing process of HPFRC-NC. The manufacturing process is described below:

The bottom layer of the partitioned steel mold was assembled and a mold releasing oil was applied. NC was then poured into the bottom layer and the assembly was vibrated for 30 s. NC was immediately covered with wet burlap and moist cured at $23 \pm 2^\circ \text{C}$. After 5–6 h of casting, the top surface of the substrate was adequately roughened to attain a sufficient bond. Upon the completion of the surface preparations, the specimens were further covered with wet burlap and left in the same curing room for 24 h. After removal of the burlap the exposed area of the top surface of the substrate was reduced to a square section of $50 \text{ mm} \times 50 \text{ mm}$ by waterproof duct tape. The reduction in the bond areas was necessary to guarantee the failure through the interface. A previous study using similar shear apparatus [35] showed the area of failure decides whether the failure will be cohesive or adhesive. The top part of the steel mold was then assembled to facilitate to cast the HPFRC on top of the NC. Before the casting of HPFRC, the NC substrate was treated by two surface preparation methods as follows:

- Case 1 (mechanical): The surface was mechanically roughened, cleaned, and made ready for casting of HPFRC.
- Case 2 (mechanical/chemical): The mechanically roughened substrate is further applied with two component epoxy-based bonding agent at a prescribed rate recommended by the manufacturer.

Finally, HPFRC was then poured at the top layer for both case I and case II. The HPFRC was poured while the bonding agent was still uncured (tacky). As soon as the casting is finished the entire assembly including the molds and bi-layer specimens was covered with wet burlap and kept in the curing room at $23 \pm 2^\circ \text{C}$. After 24 h the bi-layer specimens were removed from the molds and kept under water at 55°C in the double-walled tanks. After 24 h the specimens were removed and kept in air in the moist curing room until the day of testing. This was done to make the interface (especially the epoxy treated interface) dry before testing. A step by step information is provided in Roy [37] and Roy et al., [38]. Fig. 6(b) demonstrates the manufactured bi-layered, butterfly-shaped HPFRC-NC specimens. Fig. 7 presents the direct shear debonding experiments of the HPFRC-NC specimens. Fig. 7(a) shows the testing fixture designed by Ray et al. [35] for the butterfly-shaped concrete samples, which consists of the components of bolts, groove, stepped plates, sliding side blocks, and end blocks. Fig. 7(b) demonstrates the deployment of the concrete sample in the testing fixture, and Fig. 7(c) indicates the debonding test subjected to shear loading.

The loading speed was fixed as 0.05 mm/s . The fixture was adjusted to tightly clamp the concrete samples and prevent possible motions in other directions. HPFRC and NC were only allowed to move in the shear loading direction. Loading procedures consisted of gradually applying the shear force and the resultant displacement was reported as the output. Fig. 7(d) shows the shear debonding failure patterns of HPFRC-NC using mechanical (i.e., case 1) and mechanical/chemical (i.e., case 2) bonding techniques. Because of the butterfly-shaped design, it can be seen that the debonding failure propagated along the bonding interface in both the cases and to the NC in case 2. In particular, debonding failure in case 1 occurred on the interface. On the contrary, case 2 debonding was relatively more “in” NC because the chemical agent improved the bonding behavior.

Fig. 8 presents the debonding behaviors of HPFRC-NC under direct shear force using the interface bonding techniques case 1

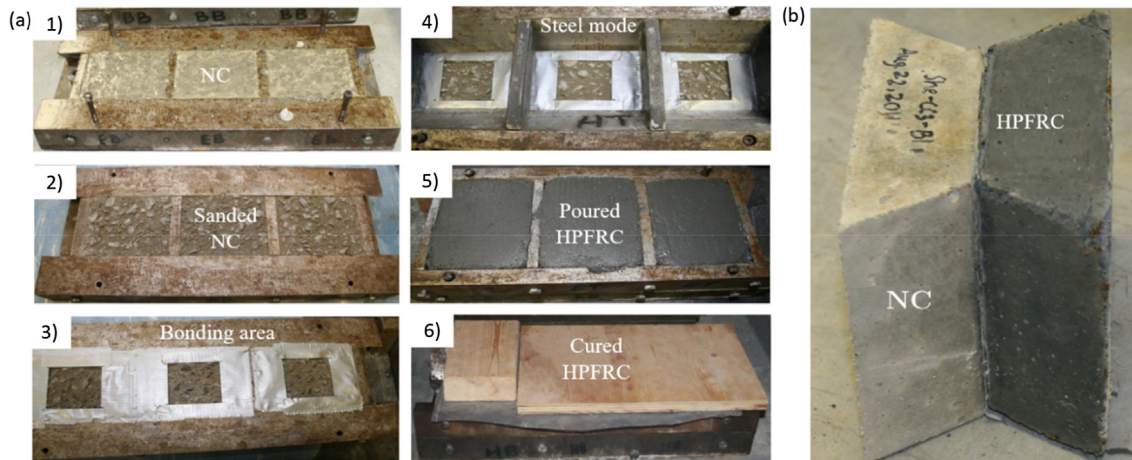


Fig. 6. (a) Manufacturing process of HPFRC-NC and (b) HPFRC-NC specimens with butterfly-shaped configuration for the direct shear test [37,38].

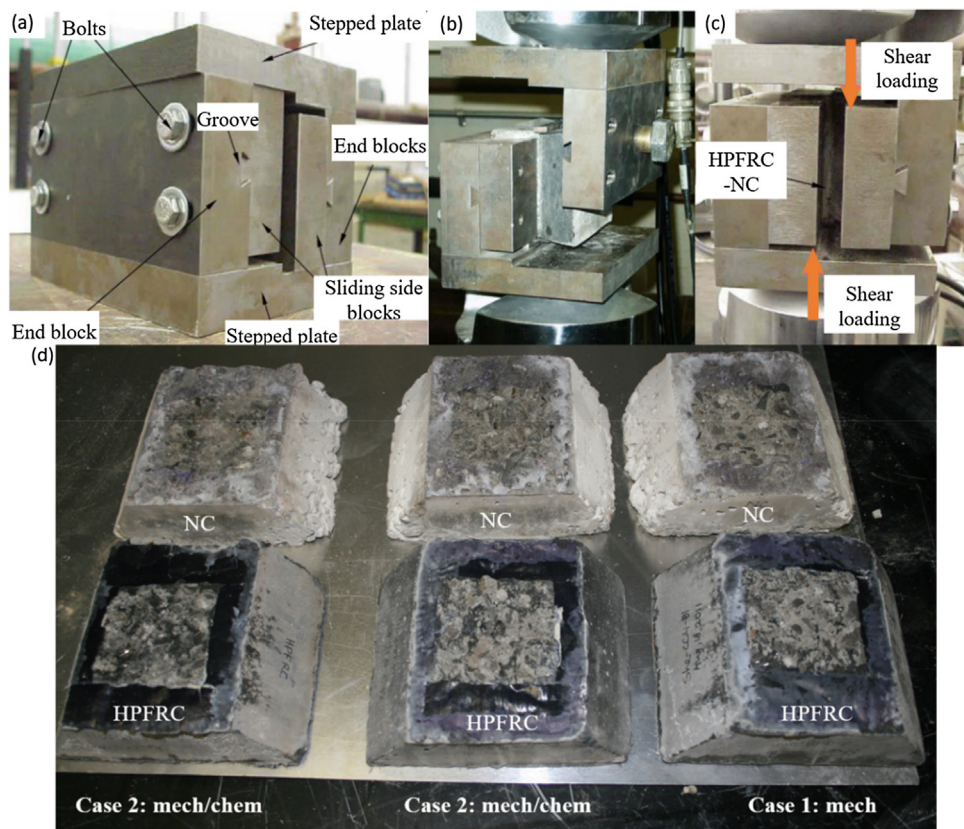


Fig. 7. (a) Fixture for the butterfly-shaped HPFRC-NC in the debonding test. (b) HPFRC-NC sample placed in the testing device. (c) Debonding test subjected to shear loading. (d) Shear debonding failure patterns of HPFRC-NC using case 1: mechanical and case 2: mechanical/chemical bonding techniques [37].

(i.e., mechanical preparation) and case 2 (i.e., mechanical/chemical preparation). The debonding response was critically “delayed” by applying the chemical bonding agent between HPFRC and NC, because the bonding interface was strengthened due to the mechanical/chemical preparation. The debonding failure went into NC (Fig. 7(d)) and thus, the peak debonding force was reduced.

3. Numerical simulations of HPFRC-NC debonding behavior

3.1. FE modeling of HPFRC-NC

Numerical simulations were conducted in Abaqus to predict the debonding behavior of HPFRC-NC. The FE model was built in the butterfly configuration (Fig. 6(b)) with the partitioned bonding

area in the middle of the interface. Following the experimental setup in Section 2, clamped boundary conditions were applied to the top and bottom surfaces of NC, while HPFRC was allowed to slide in the loading direction (i.e., z-direction). In the FE model, we assumed HPFRC to be homogeneous and the improved mechanical characteristics were determined using the experimental calibration. This is because HPFRC was completely mixed (Fig. 1(b)) to ensure the steel fibers were uniformly distributed. The geometries of the FE model were modeled the same as presented in Fig. 5(b). The element and loading conditions, and numerical solving algorithm are presented in Table 3.

HPFRC and NC were defined as plastic materials in this study, and the concrete damage plasticity (CDP) theory was particularly used to define the concrete specimens. This surface-based cohesive

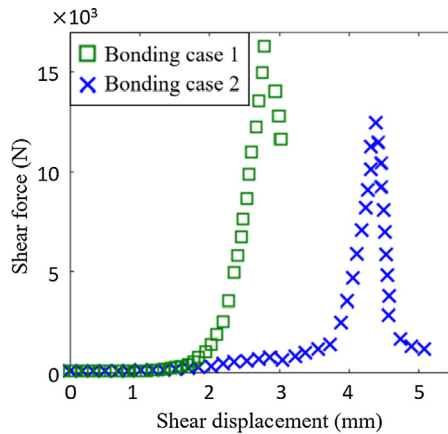


Fig. 8. Debonding response of HPFRC-NC using the bonding techniques case 1 (mechanical interface preparation) and case 2 (mechanical/chemical interface preparation).

behavior provided a simplified way to model cohesive connections using the traction-separation constitutive model. The cohesive surface behavior was defined for general contact, and the stress–strain data used in the CDP model are detailed in Appendix B. In addition, a pure master–slave formulation is enforced for surfaces with cohesive behavior to prevent over constraints. Due to the plastic deformations of the steel fibers, we defined the uniaxial response of HPFRC using the true stress–strain relationship, rather than the nominal stress–strain curve. Note that four parameters were used to describe the flow rule and yield surface in the bonding stress, including the dilation angle ϕ , plastic flow potential eccentricity ε , biaxial strength-to-uniaxial strength ratio $\frac{f_b}{f_c}$, and shape factor K . According to the calibrated results in the experiments, the fitted compressive and tensile stiffness–strain curves of HPFRC are indicated in Fig. 9. The material properties of HPFRC and NC used in the FE model are summarized in Table 4 [38,31].

Debonding behavior of HPFRC-NC was modeled using the surface-to-surface cohesive behavior with small sliding in general contact. This technique allows two bonded surfaces to deform together when the plastic displacement is within the limit state (i.e., damage evolution softening curve shown in Fig. 10). When the displacement goes beyond the limit state, the bonded surfaces start separating and thus, debonding happens to the defined surfaces. The dynamic explicit solving algorithm was applied due to the considerations of accuracy and computational cost. In particular, we obtained the same debonding results using the static, dynamic implicit and dynamic explicit solvers; however, the computational cost was significantly reduced using the dynamic explicit solving algorithm. To prevent over-constraints between the interaction of HPFRC-NC contact interface, a pure master–slave formulation was enforced for surfaces with cohesive behavior. The crack propagation of HPFRC-NC bonding interface was performed using contour integrals. The bonding surfaces before the damage evolution was defined by cohesive behavior property options, and the after evolution was defined as the damage contact. Bilinear elastic traction-separation law was used in the cohesive behavior. To ensure the mode-II shear debonding mainly occurs in the crack

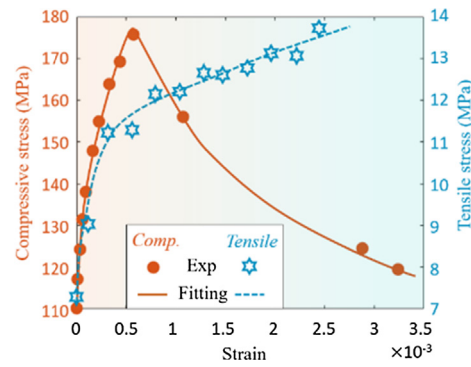


Fig. 9. Experimentally calibrated compressive (in orange) and tensile (in light blue) stress–strain data and fitting curves for HPFRC. (For interpretation of the references to colour in this figure legend, the reader is referred to the web version of this article.)

direction after damage evolution, the stiffness property in the main crack direction K_{tt} is defined larger than that in other directions (i.e., K_{nn} and K_{ss}) (see Appendix C). In addition, the maximum nominal stress criterion was applied to damage initiation.

Fig. 10 shows the hardening and softening regions in the displacement-based damage evolution softening curves of normalized shear stress vs. normalized displacement for case 1 (i.e., mechanical) and case 2 (i.e., mechanical/chemical) bonding techniques. Fig. 11(a) demonstrates the debonding failure of HPFRC-NC obtained using the FE model. The entire debonding process started from the initial status, partial debonding to complete debonding, and Fig. 11(b) displays the mesh of HPFRC-NC.

3.2. Validation of the FE model

In this section, the reported FE model is validated with the experimental results of HPFRC (presented in Fig. 4) and HPFRC-NC (presented in Fig. 8).

3.2.1. Validation of the FE model for HPFRC

The FE model of HPFRC is validated with the compressive and bending stiffnesses in the experiments. Fig. 12 indicates the comparisons of force–displacement curves between the experimental and numerical results. It can be seen that the reported numerical model accurately captures the linear increasing, dropping and linear decreasing characteristics of the compressive stiffness. The bilinear increasing and linear decreasing response of the bending stiffness is satisfactorily captured by the FE model. The satisfactory agreements between the experimental and numerical results demonstrate that the approaches used in the numerical model (e.g., dynamic explicit solver, mesh, element type, etc.) are sufficient in predicting the mechanical performance of HPFRC.

3.2.2. Validation of the debonding behavior of HPFRC-NC

This part validates the FE model of HPFRC-NC by the experimental debonding response presented in Fig. 8. Fig. 13 shows the comparisons between the numerical simulations and experimental observations. The initial stiffness K_{tt} that dominates the mode-II

Table 3
Element and loading conditions, and numerical solving algorithm in the FE model.

Element and loading				Numerical solver	
Element size of concretes (mm)	Element size of bonding area (mm)	Element type	Loading rate (mm/s)	Algorithm	Nlgeom
2	1	3D solid element (C3D8R)	0.05 in compression 0.015 in bending	Dynamic Explicit	On

Table 4
Elastic and plastic material properties in the CDP material models for HPFRC and NC.

	Density (kg/m ³)	Elasticity		Plasticity			
		Young's modulus (MPa)	Poisson's ratio	Dilation angle ϕ (°)	Eccentricity ϵ	$\frac{f_b}{f_c}$	K
HPFRC	2450	49,467	0.2	20	0.1	1.16	0.6667
NC	2400	26,480	0.167	15	0.1	1.16	0.6667

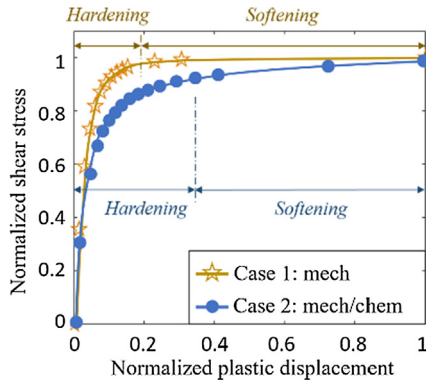


Fig. 10. Hardening and softening regions in the damage evolution softening curves for case 1 (i.e., mechanical) and case 2 (i.e., mechanical/chemical) bonding techniques.

debonding is varied, and the other two stiffnesses are maintained relatively small. Particularly, the specify stiffness coefficients for the cohesive behavior under direct shear debonding are: $K_{tt} = 117.46$ and $K_{nn} = K_{ss} = 1$ (see **Appendix C**). Good agreements are obtained from the comparisons of debonding behaviors for the bonding techniques of case 1: mechanical and case 2: mechanical/chemical.

3.3. Parametric studies on HPFRC-NC

The main goal of this study is to investigate HPFRC as a repairing material to NC. According to the numerical modelling technique used in this study (i.e., CDP material model for concrete), the dilation angle ϕ among the four plasticity parameters in the CDP material model (as summarized in **Table 4**) is particularly

studied. Therefore, the presented numerical model is used to investigate the mechanical response of HPFRC with ϕ .

Fig. 14(a) indicates the influence of the plasticity property on the compressive stiffness and **Fig. 14(b)** shows the effect on the bending stiffness. It can be seen that the maximum compressive and bending forces are reduced when the dilation angle is increased. However, the dilation angle tends not to affect the mechanical performance of HPFRC significantly. **Fig. 15** investigates the influence of the effective bonding area A_{bond} on the debonding behavior of HPFRC-NC. To numerically reveal the influence of A_{bond} on the debonding response, the bonding area ratio R_A is defined as

$$R_A = \frac{A_{bond}}{A_{cont}} \tag{1}$$

where A_{cont} denote the contact area of the surfaces between HPFRC and NC.

Fig. 15(a) displays the effect of R_A on the direct shear debonding of HPFRC-NC using the mechanical interfacial preparation method (case 1), and **Fig. 15(b)** shows the effect of R_A on that using the mechanical/chemical method (case 2). The bonding area ratio critically impacts the maximum debonding force for both of the bonding techniques, which demonstrates the significance of the bonding area A_{bond} on the debonding behavior of HPFRC-NC. Reducing the bonding area A_{bond} , however, the overall debonding pattern (i.e., force–displacement relationship) is maintained the same for the bonding case 1 and case 2.

Fig. 16 presents the maximum debonding force F_{max} of HPFRC-NC with respect to the bonding area ratio R_A and initial stiffness K_{tt} that dominates the mode-II debonding. **Fig. 16(a)** shows the discretized numerical results of F_{max} , which indicates that the debonding force is severely reduced by the decreasing of R_A . The initial stiffness K_{tt} , on the other hand, is less significant to the debonding behavior of HPFRC-NC. **Fig. 16(b)** displays a density plot of the maximum debonding force by nonlinearly fitting

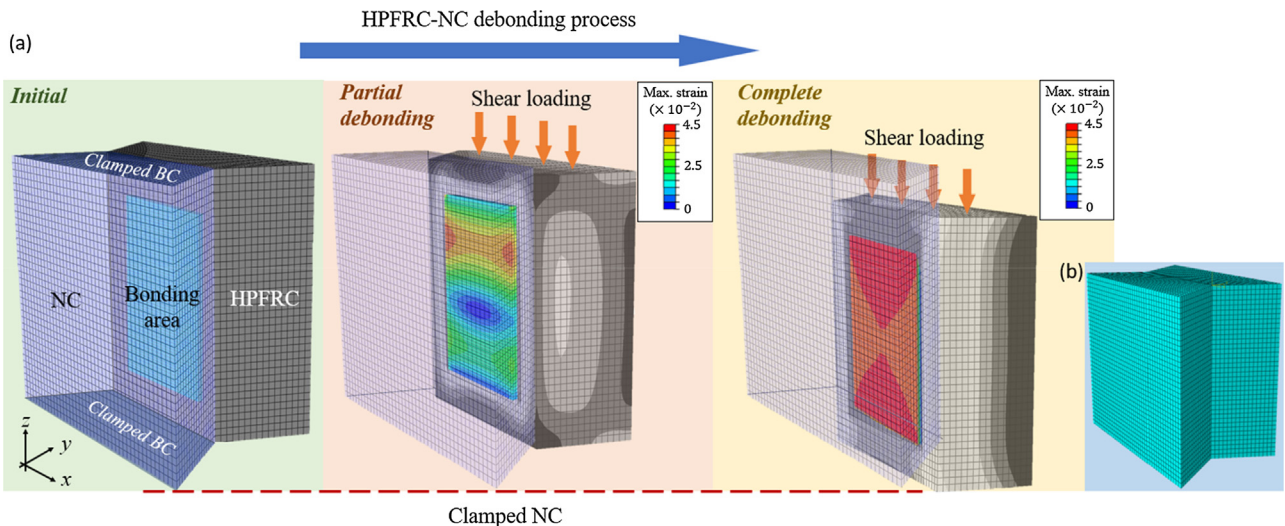


Fig. 11. (a) Debonding process of HPFRC-NC under direct shear loading in the FE model. (b) Mesh of HPFRC-NC.

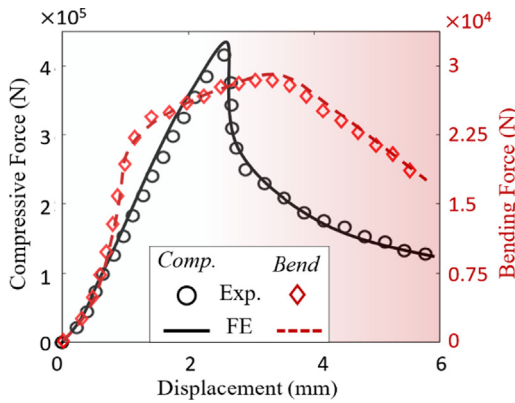


Fig. 12. Comparisons of the axial force-displacement responses of HPFRC in the compression (in black) and 3-point bonding (in red) experiments. (For interpretation of the references to colour in this figure legend, the reader is referred to the web version of this article.)

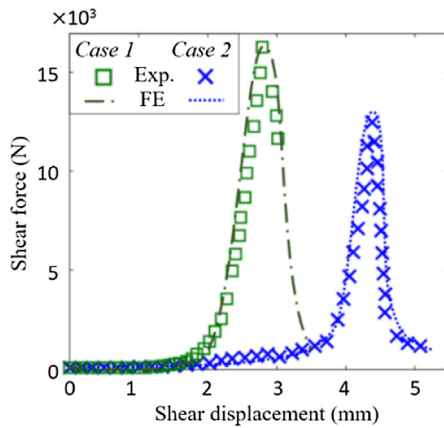


Fig. 13. Comparison of the debonding behaviors of HPFRC-NC using the bonding strategies of case 1: mechanical (in green) and case 2: mechanical/chemical (in blue). (For interpretation of the references to colour in this figure legend, the reader is referred to the web version of this article.)

the FE data in Fig. 16(a). It can be seen that the debonding behavior of HPFRC-

NC is significantly influenced by the effective bonding area A_{bond} in the contact interface between the concrete components.

4. Machine Learning-Based HPFRC-NC debonding prediction model

In this section, we study the mechanical response of HPFRC-NC using artificial intelligence-based approaches. The goal is to obtain an empirical model to predict the debonding behavior between the concrete components, and particularly to formulate the shear debonding strength. Given that HPFRC has been extensively applied as a repair material to existing concrete structures, it is of desire to achieve an accurate prediction model to optimize the bonding performance and enhance the critical debonding strength. One of the most severe issues of predicting the HPFRC-NC debonding behavior is how to characterize the dependent parameters using the most suitable simulation techniques. In this study, a robust ML algorithm called gene expression programming (GEP) is developed to derive a highly nonlinear prediction model for the shear debonding of HPFRC-NC.

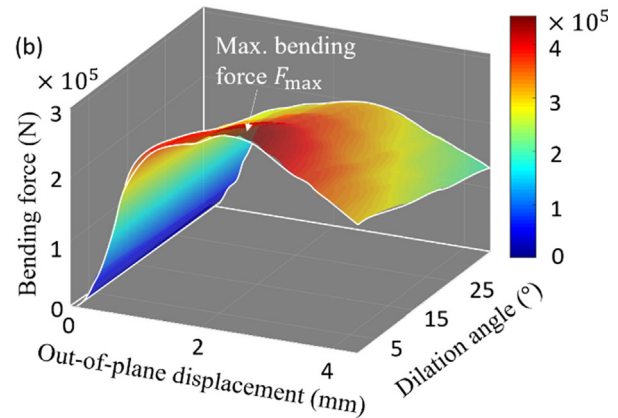
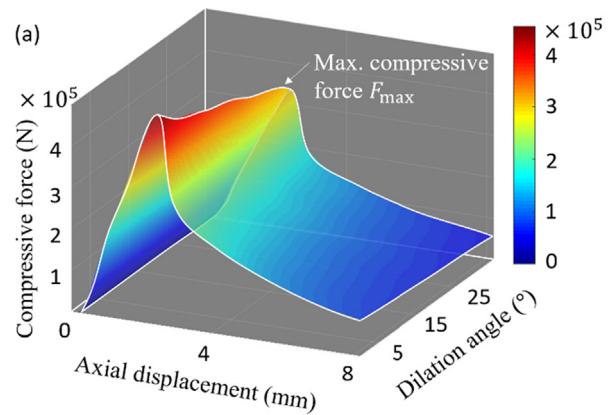


Fig. 14. Influences of dilation angle ϕ on (a) compressive stiffness and (b) bending stiffness of HPFRC.

4.1. Gene expression programming method

As a subdivision of artificial intelligence (AI) inspired by biological learning processes, the ML techniques are considered as powerful, modern alternative to traditional analysis methods to predict the behavior of real-world systems. They automatically learn from experience and extract various discriminators in the process [25]. ML has a range of well-known branches, such as the artificial neural network (ANN), fuzzy inference system (FIS), adaptive neuro-fuzzy system (ANFIS), and support vector machines (SVM). These techniques have been successfully deployed to solve problems in the engineering field (e.g., [32,53]). Among different ML techniques, ANNs are arguably the most widely used methods. Despite their good performance, ANNs are considered as black-box models. That is, they are not capable of generating practical prediction equations. Another limitation of ANNs is that their structure needs to be defined in advance as done for traditional regression [2].

Inspired by the natural evolution and the Darwinian concept of “Survival of the Fittest”, evolutionary computational (EC) methods are well-known branches of soft computing. Some of the subsets of EC are evolutionary strategies (ESs) [41] and evolutionary programming (EP) [15]. These techniques are collectively known as evolutionary algorithms (EAs). In general, an EA consists of an initial population of random individuals improved by a set of genetic operators (e.g., reproduction, mutation and recombination). The individuals are encoded solutions in form of binary strings of numbers evaluated by some fitness functions [11]. Improvement of the population is a process to reach the fittest solution with the maximum convergence. Typically, in an EA, a population of individual is randomly created and then the members are ranked according to a fitness function. The members with the highest fitness ranking are given a higher chance to become parents for the next

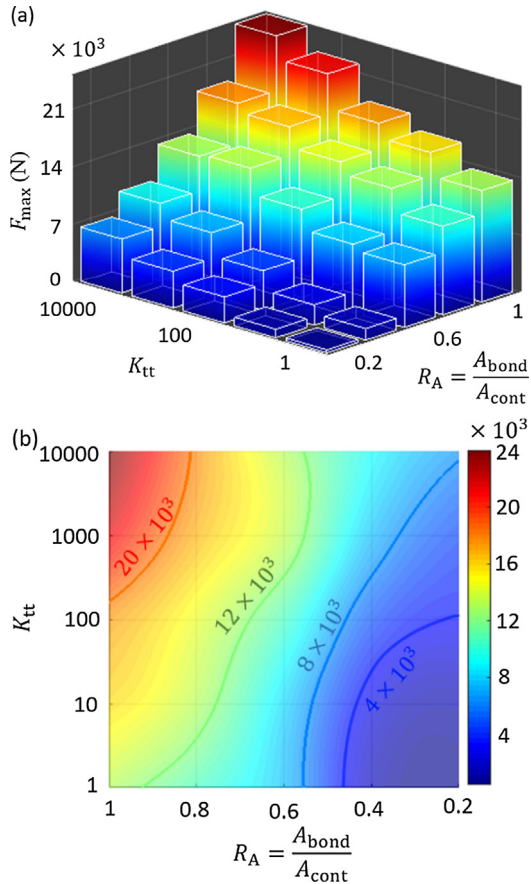


Fig. 15. (a) Variations of the maximum debonding force F_{max} with respect to the bonding area ratio R_A and initial debonding stiffness K_{tt} . (b) Nonlinearly fitted density plot of F_{max} with R_A and K_{tt} .

generation (offspring). The approach used to generate offspring from the parents is referred to as the reproduction heuristic. Then selected members are randomly transformed into new members via mutation, recombination or crossover. These steps are repeated until the convergence conditions are satisfied and the fittest member is selected [21,11]. The differences between EAs are in the way that they represent the individual structures, types of selection mechanism, forms of genetic operators, and measures of performance [4].

The genetic algorithm (GA) technique is considered as a robust EA for dealing with a wide variety of complex civil engineering problems [47,26]. Note that genetic programming (GP) is a specialization of GA where the encoded solutions (individuals) are computer programs rather than binary strings [21,8]. Fig. 17 illustrates a comparison of the encoded solutions (individuals) by GA and GP [4]. In GP, inputs and corresponding output data samples are known and the main goal is to generate predictive models relating them [48]. GP has advantages over the other ML techniques such as ANNs. A notable feature of GP and its variants is that they can produce highly nonlinear prediction equations without a need to pre-define the form of the existing relationship [2]. However, the application of GP and its variants to infrastructure condition assessment has yet to be fully exploited. The traditional tree-based GP is the mostly widely-used representation of GP [48]. The solutions evolved by the traditional GP algorithm are computer programs represented as tree-shaped structures and expressed in a functional programming language (such as LISP). Since computers do not naturally run tree-shaped programs, slow interpreters

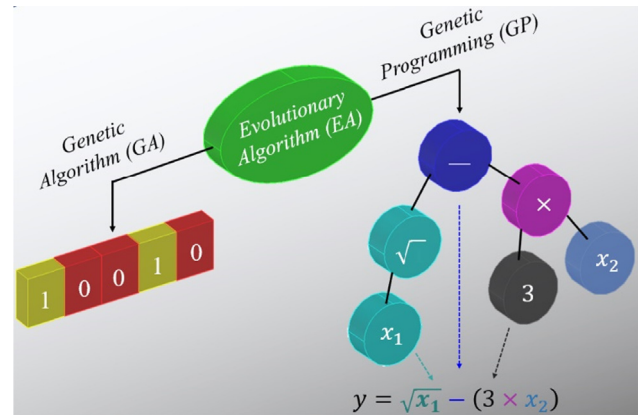


Fig. 16. A comparative illustration of encoded solutions by GA and GP.

are used as a part of the traditional GP. As a result, the simulation process using such functional programming language is slow. In addition to the traditional tree-based GP, there are other types of GP approaches, i.e., linear and graph-based [8]. The emphasis of the present study was placed on linear-based GP techniques. The programs evolved by linear variants of GP are represented as linear strings that are decoded and expressed as nonlinear entities [30]. A linear GP system can run several orders of magnitude faster than comparable tree-based interpreting systems. The enhanced speed of the linear variants of GP permits conducting many runs in realistic timeframes. This leads to deriving consistent and high-precision models with little customization.

GEP is one of the robust linear-GP techniques proposed by Ferreira [14]. While the traditional GP representation is based on the evaluation of a single tree (model) expression, GEP evolves computer programs of different sizes and shapes encoded in linear chromosomes of fixed length. The evolved programs are then expressed as parse trees of different sizes and shapes. These trees are called GEP expression trees (ETs) [2,4]. The nature of GEP allows the evolution of more complex programs composed of several subprograms. Function set, terminal set, fitness function, control parameters, and termination condition are the main components of GEP. Each GEP gene contains a list of symbols with a fixed length that can be any element from a function and terminal set. Comprehensive descriptions of the GEP algorithm can be found in [2,4]. Fig. 17 presents a comparative illustration of encoded solutions by the GA and GP algorithms.

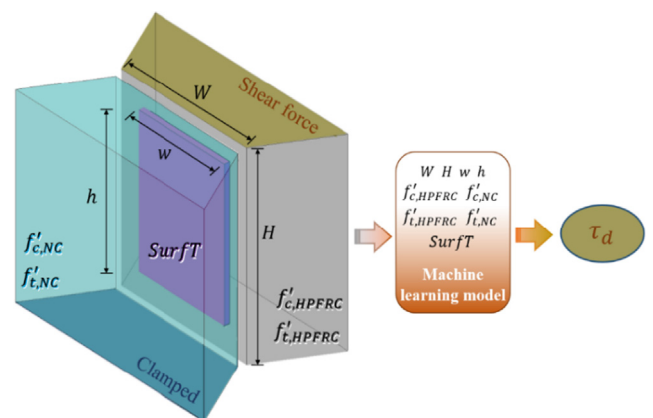


Fig. 17. Predictor variables used in the GEP model to predict the τ_d of HPFRC-NC.

4.2. GEP-Based prediction model for shear debonding of HPFRC-NC

In this study, a GEP prediction model is developed for the shear debonding strength (τ_d) of HPFRC-NC using the numerical results obtained from the FE model. Following the existing studies in the literature, the variables affecting τ_d are categorized into three groups, including the geometry, material and bonding variables [17,18,24,50,55]. In particular, the geometry variables include contact interface width W , height H , bonding area width w and height h (which are investigated in terms of the bonding area ratio R_A in Section 3.3). The compressive and tensile strengths of HPFRC and NC, $f'_{c,HPFRC}$, $f'_{t,HPFRC}$, $f'_{c,NC}$ and $f'_{t,NC}$, respectively, are used as the material factors, and the interface bonding technique *SurfT* (i.e., case 1: mechanical vs. case 2: mechanical/chemical) is also taken into account. Consequently, the GEP model that predicts τ_d can be formulated as:

$$\tau_d = f \left(\underbrace{W, H, w, h}_{\text{Geometry}}, \underbrace{f'_{c,HPFRC}, f'_{t,HPFRC}, f'_{c,NC}, f'_{t,NC}}_{\text{Material}}, \underbrace{SurfT}_{\text{Bonding}} \right) \quad (2)$$

Fig. 18 presents the variables used in the τ_d prediction model. An alternative approach is proposed for the calibration of the GEP model. Several configurations of $W, H, w, h, f'_{c,HPFRC}, f'_{t,HPFRC}, f'_{c,NC}, f'_{t,NC}$, and *SurfT* are introduced into the FE model, and the corresponding shear strength values are obtained. Subsequently, the developed database of 63 samples is used to train the GEP algorithm. The proposed strategy is particularly important because performing laboratory testing to determine the shear strength of HPFRC-NC is costly and time-consuming. In addition, the numerical approach readily provides the opportunity to investigate the effect of various scenarios affecting the shear strength. The database of the maximum shear debonding stress and ranges of the variables used to develop the GEP model are summarized in Appendix D.

In the analysis, *SurfT* type is represented by 1 for mechanical bonding surface treatment without chemical agent and 2 for mechanical bonding surface treatment with chemical agent. For the GEP analysis, three random divisions were considered for the data: learning (~65%), validation (~10%), and testing (~25%) [8,12,29,7]. The learning and validation subsets were used to calibrate and evaluate the models, respectively. Since they were both involved in selecting the final models, they were labeled as training data in the subsequent analyses. After a series of preliminary runs and observing the GEP algorithm performance, it is found that all of the considered variables (i.e. $W, H, w, h, f'_{c,HPFRC}, f'_{t,HPFRC}, f'_{c,NC}, f'_{t,NC}$, and *SurfT*) improve the prediction performance. Then, the GEP method is used to explore the best mathematical models.

Table 5 shows a set of parameters used in the GEP simulations. The values considered for these parameters were based on both some previously suggested values [2,1] and after making several preliminary runs and observing the performance behavior. There are five main parts for setting GEP parameters including: general setting, complexity increase, genetic operators, numerical constant, and fitness function. Several runs were conducted to come up with a parameterization of GEP that provided enough robustness and generalization to solve the problem. Three levels were set for the population size (number of chromosomes) (20, 40, 80). The chromosome architectures of the models evolved by GEP include head size and number of genes. The success of the GEP algorithm usually increases with increasing the initial and maximum program size parameters. In this case, the complexity of the evolved functions increases. Three optimal levels were considered for the head size (2, 4, 6) and three levels were set for the number of genes (6, 8, 10). For the number of genes greater than

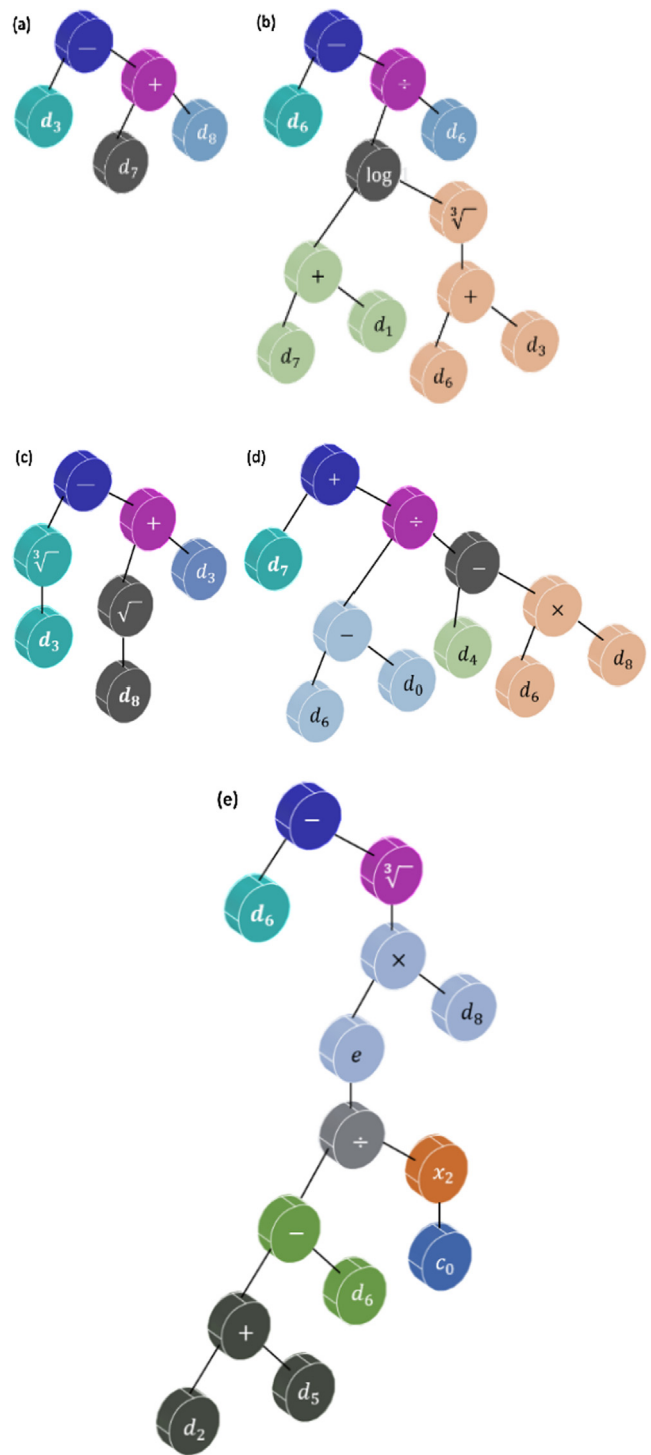


Fig. 18. Expression trees of the best GEP prediction model on τ_d (ET = \sum Sub-ET_i) for (a) ET₁, (b) ET₂, (c) ET₃, (d) ET₄, and (e) ET₅.

one, the addition linking function was used to link the mathematical terms encoded in each gene. There were $3 \times 3 \times 3 = 27$ different combinations of the parameters. All of these parameter combinations were tested, and 3 replications are carried out for each of them. Therefore, the overall number of optimal individual runs was equal to $27 \times 3 = 81$. The period of time acceptable for evolution to occur without improvement in best fitness is set via the generations without change parameter. After 2000 generations, a mass extinction or a neutral gene was automatically added to the model. The program was run until no longer significant improve-

Table 5
Parameter settings for the GEP algorithm.

Category	Parameter	Settings
General	Chromosomes	20, 40, 80
	Genes	2, 4, 6
	Head Size	6, 8, 10
	Linking Function	Addition
	Function set	+, -, ×, /, √, √3, log, power, exp
Complexity Increase	Generations without Change	2000
	Number of Tries	3
	Max. Complexity	5
Genetic Operators	Mutation Rate	0.00138
	Inversion Rate	0.00546

ment is obtained from the model. The GEP algorithm was implemented using GeneXproTools.

The optimal GEP-based prediction model for the τ_d of HPFRC-NC is:

$$\tau_d(\text{MPa}) = -\text{SurfT} - \sqrt{\text{SurfT}} + \sqrt[3]{h} + \sqrt[3]{e^{\frac{w \cdot f'_{c,NC} - f'_{t,HPFRC}}{27.924}} \times \text{SurfT}} + \frac{f'_{t,HPFRC} - W}{f'_{c,HPFRC} - (f'_{t,HPFRC} \times \text{SurfT})} - \frac{\text{Log}(f'_{t,NC} + H)}{f'_{t,HPFRC} \times \text{Log}(\sqrt[3]{f'_{t,HPFRC}} + f'_{c,NC})} \quad (3)$$

where, $W, H, w, h, f'_{c,HPFRC}, f'_{t,HPFRC}, f'_{c,NC}, f'_{t,NC}$, and SurfT denote the contact interface width, contact interface height, bonding area width, bonding area height, compressive strengths of HPFRC, tensile strengths of HPFRC, compressive strengths of NC, tensile strengths of NC, and interface bonding strategy, respectively. In Eq. (3), SurfT is varied between 1 and 2, where 1 denotes mechanical surface treatment and 2 represents mechanical/chemical surface treatment. As seen, the model is a complicated combination of parameters and operators to predict τ_d . It is generated by the GEP algorithm after controlling millions of linear and nonlinear models. Thus, it can efficiently consider the interactions between the predictor variables and τ_d .

The expression trees (ETs) of the obtained model is given in Fig. 19. In this figure, d_0, \dots, d_8 represent $W, H, w, h, f'_{c,HPFRC}, f'_{t,HPFRC}, f'_{c,NC}, f'_{t,NC}$, and SurfT , respectively, and parameter c_0 is a numerical constant. This model is comprised of five individual sub-models connected using addition operation. Each of these sub-models includes a part of the information provided by the final model [14]. Fig. 20 presents the predictions provided by this model. The high density of the points around the ideal 45-degree angle line clearly indicates the good performance of the model. Determination coefficient (R^2), root mean squared error (RMSE) and mean absolute error (MAE) are used as the performance measures.

One of the advantages of GEP for predicting τ_d is that it directly learns from raw experimental data presented to it. This method extracts the subtle functional relationships among the data, even if the underlying relationships are unknown or the physical meaning is difficult to be explained. Contrary to GEP and other GP branches, most conventional methods (like regression and finite element method) need prior knowledge about the nature of the relationships among the data. Classical constitutive models rely on assuming the structure of the model in advance, which may be suboptimal. On the other hand, the best solutions generated by GEP are determined after controlling numerous preliminary models, even millions of linear and nonlinear models. Therefore,

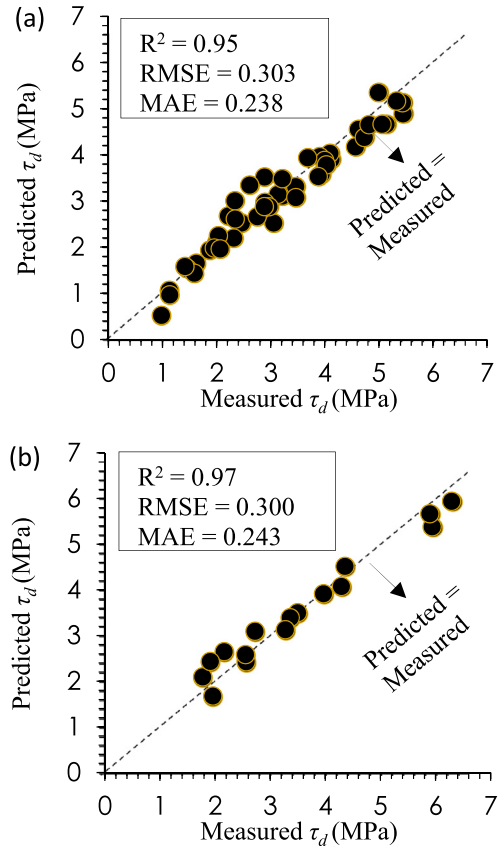


Fig. 19. Measured against predicted τ_d using the GEP model: (a) training data, (b) testing data.

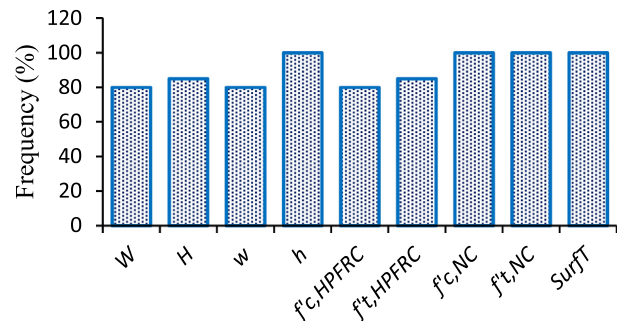


Fig. 20. Sensitivity analysis of the final predictor variables in the GEP analysis.

the beauty of the derived model is that it can efficiently consider the interactions between the dependent and independent variables.

4.3. Design example

The proposed GEP model is used to predict the experimental τ_d of two HPFRC-NC samples reported by Manish et al. (2014).

Sample 1

$W = 75$ mm, $H = 102$ mm, $w = 50$ mm, $h = 50$ mm, $f'_{c,HPFRC} = 108.6$ MPa, $f'_{t,HPFRC} = 40$ MPa, $f'_{c,NC} = 13.5$ MPa, $f'_{t,NC} = 5$ MPa, and $\text{SurfT} = 1$ (i.e., mechanical bonding treatment).

Table 6
Performance measures for further validation of the GEP model.

Item	Formula	Condition	GEP
1	$R = \frac{\sum_{i=1}^n (O_i - \bar{O}_i)(t_i - \bar{t}_i)}{\sqrt{\sum_{i=1}^n (O_i - \bar{O}_i)^2 \sum_{i=1}^n (t_i - \bar{t}_i)^2}}$	$0.8 < R$	0.985
2	$k = \frac{\sum_{i=1}^n (h_i \times t_i)}{h_i^2}$	$0.85 < k < 1.15$	1.014
3	$k' = \frac{\sum_{i=1}^n (h_i \times t_i)}{t_i^2}$	$0.85 < k' < 1.15$	0.981
4	$m = \frac{R^2 - R_o^2}{R^2}$	$ m < 0.1$	-0.030
5	$n = \frac{R^2 - R_o'^2}{R^2}$	$ n < 0.1$	-0.030
6	$R_m = R^2 \times \left(1 - \sqrt{R^2 - R_o'^2}\right)$	$0.5 < R_m$	0.804
7	$R_o^2 = 1 - \frac{\sum_{i=1}^n (t_i - h_i^0)^2}{\sum_{i=1}^n (t_i - \bar{t}_i)^2}, h_i^0 = k \times t_i$	Should be close to 1	0.999
8	$R_o'^2 = 1 - \frac{\sum_{i=1}^n (h_i - t_i^0)^2}{\sum_{i=1}^n (h_i - \bar{h}_i)^2}, t_i^0 = k' \times h_i$	Should be close to 1	0.997

Sample 2

$W = 75$ mm, $H = 102$ mm, $w = 50$ mm, $h = 50$ mm, $f'_{c,HPFRC} = 90$ MPa, $f'_{t,HPFRC} = 30$ MPa, $f'_{c,NC} = 11$ MPa, $f'_{t,NC} = 4$ MPa, and $SurfT = 2$ (i.e., mechanical/chemical bonding treatment).

Substituting these numbers into Eq. (3), the predicted τ_d values for Sample 1 and Sample 2 are 3.28 and 1.89 MPa, respectively. The measured τ_d values for Sample 1 and Sample 2 are 3.2 and 2.1 MPa, which are 2% lower and 10% higher than the predicted τ_d , respectively.

4.4. Performance evaluation

On the basis of a rational hypothesis, Smith [42] argues that for the correlation coefficient ($|R|$) higher than 0.8, a strong correlation exists between the predicted and measured values. In all conditions, the error values (e.g. RMSE or MAE) should be maintained as the minimum [1]. Based on the results shown in Fig. 20, the proposed GEP model has a satisfactory performance on the training and testing data sets. As observed from Table 6, the developed model satisfies all of the requisite conditions, and the validation phase ensures that the proposed models are strongly suitable and applicable.

4.5. Sensitivity analysis

As discusses in Section 4.2, an extensive simulation study is carried out to find the most relevant parameters such that to develop the most effective prediction model. The optimal models are built using 9 input parameters ($W, H, w, h, f'_{c,HPFRC}, f'_{t,HPFRC}, f'_{c,NC}, f'_{t,NC}$, and $SurfT$). However, a second phase of sensitivity analysis is further performed to distinguish the parameters with higher contributions in the final models. To this aim, the frequency values of the input parameters are obtained for the GEP models. In case a design variable has appeared in 100% of the best thirty GEP programs, its frequency value will be equal to 100 [16]. Fig. 21 shows the GEP sensitivity analysis results. As seen, τ_d is more sensitive to $h, f'_{c,NC}, f'_{t,NC}$, and $SurfT$ compared to the other variables.

5. Conclusions

This paper reported HPFRC as a repairing material for NC and particularly investigated the debonding behavior between HPFRC and NC under direct shear loading. The HPFRC specimens were first

fabricated and calibrated to obtain the compressive and bending (i.e., flexural) strengths. The HPFRC-NC samples were then experimentally made using the bonding techniques of the mechanical surface treatments with and without chemical agent. A FE model was developed to characterize the debonding behavior of HPFRC-NC with different geometric and material parameters and the bonding interface treatments. A powerful ML method called GEP was then deployed to develop a prediction model for the shear strength of HPFRC-NC. An alternative approach was proposed for the calibration of the GEP model. The obtained numerical results were used to train the GEP algorithm. Design examples were presented to illustrate the efficiency of the developed GEP model in characterizing the mechanical response of the HPFRC-NC samples. One of the distinctive features of GEP-based model is that it is established upon the experimental data rather than on the assumptions made in developing the conventional models. The predictive capabilities of the derived model is within the range of the data used for its calibration. However, the model can easily be retrained and improved to make more accurate predictions for a wider range by including the data for other material types and testing conditions. However, the GEP algorithm is parameter sensitive. The GEP simulation process can be accelerated via using any form of optimally controlling the parameters of the run. In this context, further research can focus on hybridizing GEP with optimization algorithms such as GAs, Simulated Annealing, Ant Colony, or Tabu Search. Future research can also focus on studying the debonding behavior of other types of high-performance concretes as repairing materials to NC structures.

Declaration of Competing Interest

The authors declare that they have no known competing financial interests or personal relationships that could have appeared to influence the work reported in this paper.

Acknowledgements

This study is partially supported by the Startup Foundation of the Hundred Talented Program at the Zhejiang University. The experimental portion of the work was performed at the West Virginia University, Morgantown, WV with the financial support from West Virginia EPSCoR. The authors are grateful to Dr. David B. DeVallance and Dr. Brijesh Mishra (West Virginia University) and his students (Mr. Diachao Nie and Mr. Priyesh Verma) and Prof. J.F. Davalos (the City University of New York) for technical support in the experiments.

Appendix

A. Component material properties of HPFRC

Table A1 displays the compound compositions of the Portland cement. Table A2 presents the sieve analysis data of the sands. Table A3 summarizes the geometric and material properties of the steel fibers. Table A4 shows the analysis data for ultrafine quartz powder. Table A5 exhibits the basic properties and major chemical compositions of silica fume (SF).

B. Detailed information in the FE model

Table B1 presents the compressive and tensile stress-strain data used to characterize the mechanical properties of HPFRC in

Table A1
Compound compositions of Portland cement [37].

Compounds	SiO ₂	CaO	Al ₂ O ₃	Fe ₂ O ₃	MgO	SO ₃	LOI	Na ₂ O + 0.658K ₂ O	C ₃ A	C ₃ S	Insoluble residue
% by mass	20.2	63.6	5.4	4.3	0.94	3.0	1.35	0.56	7.2	54.0	0.3

Table A2
Sieve analysis data for fine natural sands [37].

Sieve size (mm)		0.85	0.6	0.42	0.3	0.25	0.21	0.15
% passing (by wt.)	Sand OO	100	95	40	5	2	1	–
	Sand OOO	100	100	95	75	45	30	5

Table A3
Geometric and material properties of steel fibers [37].

Properties	Length (mm)	Diameter (mm)	Aspect ratio	Tensile strength (GPa)	Young's modulus (GPa)	Specific gravity
Values	13	0.2	65	2.16	210	7.85

Table A4
Sieve analysis data for ultrafine quartz powder [37].

Sieve size (mm)		0.15	0.106	0.075	0.053	0.045
% passing (by wt.)		100.0	99.8	97.3	88.8	82.3

Table A5
Basic properties and major chemical compositions of silica fume (SF) [37].

Properties	Specific gravity	SiO ₂ (%)	Crystalline SiO ₂ (%)
Values	2.2	60–100	0.5–1.5

$$\mathbf{t} = \begin{bmatrix} t_n \\ t_s \\ t_t \end{bmatrix} = \begin{bmatrix} K_{nn} & K_{ns} & K_{nt} \\ K_{ns} & K_{ss} & K_{st} \\ K_{nt} & K_{st} & K_{tt} \end{bmatrix} \begin{bmatrix} \delta_n \\ \delta_s \\ \delta_t \end{bmatrix} = \mathbf{K}\delta \quad (C1)$$

where $K_{ns} = K_{sn} = K_{nt} = K_{tn} = K_{st} = K_{ts} = 0$. Due to the mode-II debonding of HPFRC-NC under direct shear loading, K_{tt} is dominant in the stiffness matrix. Therefore, the debonding behavior between HPFRC and NC is investigated in terms of K_{tt} .

the CDP model. Table B2 presents the compressive and tensile stress–strain data used in the CDP model for NC.

C. Definition of the initial stiffness \mathbf{K}

The coefficients in the initial stiffnesses K_{nn} , K_{ss} and K_{tt} are defined as

D. FE data of the maximum shear debonding stress

Table D1 summarizes the database used in the machine learning model with respect to predictor variables. Table D2 details the ranges of the variables.

Table B1
Compressive and tensile stress–strain data in the CDP model for HPFRC.

Comp.	Stress	110.2	117.2	124.3	131.4	138.0	147.9	154.9	163.9	169.2	175.7	156.0	124.5	119.2
	Strain	0	9E-6	3.5E-5	5.8E-5	9.3E-5	1.6E-4	2.3E-4	3.3E-4	4.4E-4	5.7E-4	1.1E-3	2.9E-3	3.3E-9
Tensile	Stress	7.42	9.12	11.24	11.33	12.14	12.22	12.65	12.6	12.78	13.11	13.05	13.7	–
	Strain	0	1.2E-4	3.2E-4	5.7E-4	8E-4	1.1E-3	1.3E-3	1.5E-3	1.7E-3	2E-3	2.2E-3	2.5E-3	–

Table B2
Compressive and tensile stress–strain data in the CDP model for NC.

Comp.	Stress	24.02	29.21	31.71	32.36	31.77	30.38	28.51	21.91	14.9	2.95
	Strain	0	4E-4	8E-4	1.2E-3	1.6E-3	2E-3	2.4E-3	3.6E-3	5E-3	1E-2
Tensile	Stress	1.78	1.46	1.11	0.96	0.8	0.54	0.36	0.16	0.07	0.04
	Strain	0	1E-4	3E-4	4E-4	5E-4	8E-4	1E-3	2E-3	3E-3	5E-3

Table D1
Database of the τ_d of HPFRC-NC and associated predictor variables.

Trail No.	Geometry Variables (mm)				Material Variables (MPa)				Bonding variable <i>SurfT</i>	Debonding behavior (MPa) τ_d
	<i>W</i>	<i>H</i>	<i>w</i>	<i>h</i>	$f'_{c,HPFRC}$	$f'_{c,NC}$	$f'_{t,HPFRC}$	$f'_{t,NC}$		
1	50	70	40	40	50	16	5	1.5	Mech.*	1.412
2	55	80	50	50	50	16	5	1.5	Mech.	1.954
3	60	90	64	64	50	16	5	1.5	Mech.	2.548
4	70	95	70	80	50	16	5	1.5	Mech.	2.968
5	75	102	75	102	50	16	5	1.5	Mech.	3.459
6	50	70	40	40	65	20	7.3	2.1	Mech.	1.772
7	55	80	50	50	65	20	7.3	2.1	Mech.	2.457
8	60	90	64	64	65	20	7.3	2.1	Mech.	3.134
9	70	95	70	80	65	20	7.3	2.1	Mech.	3.212
10	75	102	75	102	65	20	7.3	2.1	Mech.	3.681
11	50	70	40	40	80	25	9.5	3	Mech.	1.909
12	55	80	50	50	80	25	9.5	3	Mech.	2.883
13	60	90	64	64	80	25	9.5	3	Mech.	3.877
14	70	95	70	80	80	25	9.5	3	Mech.	4.115
15	75	102	75	102	80	25	9.5	3	Mech.	4.731
16	50	70	40	40	90	30	11	4	Mech.	2.161
17	55	80	50	50	90	30	11	4	Mech.	3.217
18	60	90	64	64	90	30	11	4	Mech.	4.028
19	70	95	70	80	90	30	11	4	Mech.	4.567
20	75	102	75	102	90	30	11	4	Mech.	5.059
21	50	70	40	40	108.6	40	13.5	5	Mech.	2.338
22	55	80	50	50	108.6	40	13.5	5	Mech.	3.493
23	70	95	70	80	108.6	40	13.5	5	Mech.	4.818
24	75	102	75	102	108.6	40	13.5	5	Mech.	5.327
25	50	70	40	40	130	50	15	5.5	Mech.	2.612
26	55	80	50	50	130	50	15	5.5	Mech.	3.997
27	60	90	64	64	130	50	15	5.5	Mech.	5.134
28	70	95	70	80	130	50	15	5.5	Mech.	5.436
29	75	102	75	102	130	50	15	5.5	Mech.	5.892
30	50	70	40	40	140	55	15	5.5	Mech.	2.884
31	55	80	50	50	140	55	15	5.5	Mech.	4.287
32	60	90	64	64	140	55	15	5.5	Mech.	5.447
33	70	95	70	80	140	55	15	5.5	Mech.	5.935
34	75	102	75	102	140	55	15	5.5	Mech.	6.286
35	50	70	40	40	50	16	5	1.5	Mech. + Chem.**	0.977
36	55	80	50	50	50	16	5	1.5	Mech. + Chem.	1.132
37	60	90	64	64	50	16	5	1.5	Mech. + Chem.	1.624
38	70	95	70	80	50	16	5	1.5	Mech. + Chem.	2.064
39	75	102	75	102	50	16	5	1.5	Mech. + Chem.	2.558
40	50	70	40	40	65	20	7.3	2.1	Mech. + Chem.	1.126
41	55	80	50	50	65	20	7.3	2.1	Mech. + Chem.	1.457
42	60	90	64	64	65	20	7.3	2.1	Mech. + Chem.	2.031
43	70	95	70	80	65	20	7.3	2.1	Mech. + Chem.	2.342
44	75	102	75	102	65	20	7.3	2.1	Mech. + Chem.	2.719
45	50	70	40	40	80	25	9.5	3	Mech. + Chem.	1.587
46	55	80	50	50	80	25	9.5	3	Mech. + Chem.	1.871
47	60	90	64	64	80	25	9.5	3	Mech. + Chem.	2.217
48	70	95	70	80	80	25	9.5	3	Mech. + Chem.	3.464
49	75	102	75	102	80	25	9.5	3	Mech. + Chem.	3.932
50	50	70	40	40	90	30	11	4	Mech. + Chem.	1.954
51	55	80	50	50	90	30	11	4	Mech. + Chem.	2.315
52	60	90	64	64	90	30	11	4	Mech. + Chem.	2.889
53	70	95	70	80	90	30	11	4	Mech. + Chem.	3.358
54	75	102	75	102	90	30	11	4	Mech. + Chem.	3.963
55	50	70	40	40	108.6	40	13.5	5	Mech. + Chem.	2.001
56	55	80	50	50	108.6	40	13.5	5	Mech. + Chem.	2.748
57	70	95	70	80	108.6	40	13.5	5	Mech. + Chem.	3.908
58	75	102	75	102	108.6	40	13.5	5	Mech. + Chem.	4.351
59	50	70	40	40	130	50	15	5.5	Mech. + Chem.	3.055
60	55	80	50	50	130	50	15	5.5	Mech. + Chem.	3.271
61	60	90	64	64	130	50	15	5.5	Mech. + Chem.	4.095
62	70	95	70	80	130	50	15	5.5	Mech. + Chem.	4.622
63	75	102	75	102	130	50	15	5.5	Mech. + Chem.	4.989

* Mech.: Mechanical bonding surface treatment without chemical agent.

** Mech. + Chem.: Mechanical bonding surface treatment with chemical agent.

Table D2

Ranges of the variables in the GEP prediction model.

Variable	Range
Contact interface width, W (mm)	50–75
Contact interface height, H (mm)	70–102
Bonding area width, w (mm)	40–75
Bonding area height, h (mm)	40–102
Compressive strength of HPFRC, $f'_{c,HPFRC}$ (MPa)	50–140
Tensile strength of HPFRC, $f'_{t,HPFRC}$ (MPa)	5–15
Compressive strength of NC, $f'_{c,NC}$ (MPa)	16–55
Tensile strength of NC, $f'_{t,NC}$ (MPa)	1.5–5.5
Surface treatment, $SurfT$	Mech. and Mech. + Chem.
Shear debonding strength, τ_d (MPa)	0.98–6.29

References

- [1] A.H. Alavi, A.H. Gandomi, H.C. Nejad, A. Mollahasani, A. Rashed, Design equations for prediction of pressuremeter soil deformation moduli utilizing expression programming systems, *Neural Comput Appl* 23 (2013) 1771–1786.
- [2] A.H. Alavi, A.H. Gandomi, A robust data mining approach for formulation of geotechnical engineering systems, *Eng Comput* 28 (2011) 242–274.
- [3] A.H. Alavi, P. Jiao, W.G. Buttler, N. Lajnef, Internet of Things-enabled smart cities: State-of-the-art and future trends, *Meas* 129 (2018) 589–606.
- [4] A.H. Alavi, H. Hasni, N. Lajnef, K. Chatti, F. Faridazar, Damage detection using self-powered wireless sensor data: an evolutionary approach, *Meas* 82 (2016) 254–283.
- [5] M.A. Al-Osta, M.N. Isa, M.H. Baluch, M.K. Rahman, Flexural behavior of reinforced concrete beams strengthened with ultra-high performance fiber reinforced concrete, *Construct Build Mater* 134 (2017) 279–296.
- [6] H. Aoude, F.P. Dagenais, R.P. Burrell, M. Saatcioglu, Behavior of ultra-high performance fiber reinforced concrete columns under blast loading, *Int J Impact Eng* 80 (2015) 185–202.
- [7] S.K. Babanajad, A.H. Gandomi, A.H. Alavi, New prediction models for concrete ultimate strength under true-triaxial stress states: an evolutionary approach, *Advances in Engineering Software* 110 (2017) 55–68.
- [8] W. Banzhaf, P. Nordin, R.F. Keller Francone, Genetic programming: an introduction on the automatic evolution of computer programs and its application, Morgan Kaufmann, 1998.
- [9] A. Behnood, V. Behnood, M.M. Gharehveran, K.E. Alyamac, Prediction of the compressive strength of normal and high-performance concretes using M5P model tree algorithm, *Construct Build Mater* 142 (2017) 199–207.
- [10] W. Borchani, P. Jiao, R. Burgueno, N. Lajnef, Control of postbuckling mode transitions using assemblies of axially loaded bilaterally constrained beams, *J Eng Mech* 143 (10) (2017) 04017116.
- [11] C.C.A. Coello, G.B. Lamont, D.A. Van Veldhuizen, Evolutionary algorithms for solving multi-objective problems, *Genetic and Evolutionary Computation*, 2nd ed., Springer, New York, 2007.
- [12] S.K. Das, Artificial neural networks in geotechnical engineering: modeling and application issues, *Metaheuristics in Water, geotechnical and transport engineering*, Yang XS, Gandomi AH, Talatahari S, Alavi AH, editors, Elsevier, London, 2013.
- [13] B. Ellis, D.L. McDowell, M. Zhou, Energy dissipation in ultra-high performance fiber-reinforced concrete (UHPFRC) subjected to rapid loading, *AIP Conf Proc* 1426 (2012) 1061.
- [14] C. Ferreira, Gene expression programming: a new adaptive algorithm for solving problems, *Complex Syst* 13 (2001) 87–129.
- [15] L.J. Fogel, A.J. Owens, M.J. Walsh, Artificial Intelligence through Simulated Evolution, Wiley, New York, 1996.
- [16] A.H. Gandomi, A.H. Alavi, M.G. Sahab, New formulation for compressive strength of CFRP confined concrete cylinders using linear genetic programming, *Mater Struct* 43 (7) (2010) 963–983.
- [17] A.H. Gandomi, A.H. Alavi, G.J. Yun, Nonlinear modeling of shear strength of SFRC beams using linear genetic programming, *Struct Eng Mech* 38 (1) (2011) 1–25.
- [18] S.M. Hamze-Ziabari, A. Yasavoli, Predicting bond strength between FRP plates and concrete substrate: applications of GMDH and MNL approaches, *J Adv Concrete Tech.* 15 (2017) 644–661.
- [19] M.M. Hosinieh, H. Aoude, W.D. Cook, D. Mitchell, Behavior of ultra-high performance fiber reinforced concrete columns under pure axial loading, *Eng Struct* 99 (2015) 388–401.
- [20] C.C. Hung, H. Li, H.C. Chen, High-strength steel reinforced squat UHPFRC shear walls: Cyclic behavior and design implications, *Eng Struct* 141 (2017) 59–74.
- [21] J. Koza, Genetic Programming, on the programming of Computers by Means of Natural Selection, MIT Press, Cambridge (MA), 1992.
- [22] D.J. Lary, A.H. Alavi, A.L. Walker, A.H. Gandomi, Machine learning in geosciences and remote sensing, *Geosci. Front* 7 (1) (2016) 3.
- [23] X. Li, J. Wang, Y. Bao, G. Chen, Cyclic behavior of damaged reinforced concrete columns repaired with high-performance fiber-reinforced cementitious composite, *Eng Struct* 136 (2017) 26–35.
- [24] I. Mansouri, O. Kisi, Prediction of debonding strength for masonry elements retrofitted with FRP composites using neuro fuzzy and neural network approaches, *Compos B* 70 (2015) 247–255.
- [25] T. Mitchell, Does machine learning really work?, *AI Mag* 18 (3) (1997) 11–20.
- [26] E. Momeni, R. Nazir, D. Jahed Armaghani, H. Maizir, Prediction of pile bearing capacity using a hybrid genetic algorithm-based ANN, *Meas* 57 (2014) 122–131.
- [27] S.M. Mousavi, P. Aminian, A.H. Gandomi, A.H. Alavi, H. Bolandi, A new predictive model for compressive strength of HPC using gene expression programming, *Adv Eng Software* 45 (1) (2012) 105–114.
- [28] S. Mousseau, P. Paultre, J. Mazars, Seismic performance of a full-scale, reinforced high-performance concrete building. Part II: Analytical study, *Can. J Civ Eng* 35 (2008) 849–862.
- [29] P.K. Muduli, S.K. Das, S. Bhattacharya, CPT-based probabilistic evaluation of seismic soil liquefaction potential using, multi-gene genetic programming, *Georisk* 8 (1) (2014) 14–28.
- [30] M. Oltean, C. Grossan, A comparison of several linear genetic programming techniques, *Adv Complex Syst* 14 (4) (2003) 1–29.
- [31] H.A.B. Othman, Performance of ultra-high performance fiber reinforced concrete plates under impact loads PhD dissertation, Ryerson University, 2016.
- [32] J.C. Patra, An artificial neural network-based smart capacitive pressure sensor, *Meas* 22 (1997) 113–121.
- [33] M. Poubaba, E. Asefi, H. Sadaghian, A. Mirmiran, Effect of age on the compressive strength of ultra-high-performance fiber-reinforced concrete, *Construct Build Mater* 175 (2018) 402–410.
- [34] F.K.F. Radtke, A. Simone, L.J. Sluys, A computational model for failure analysis of fiber reinforced concrete with discrete treatment of fibers, *Eng Fract Mech* 77 (2010) 597–620.
- [35] I. Ray, J.F. Davalos, Z. Sun, Design of experiment and statistical analysis of bond strength test of bi-layer concrete, *Int. J. Mater. Prod. Technol.* 39 (3–4) (2010) 302–316.
- [36] M. Roy, C. Hollmann, K. Wille, Influence of volume fraction and orientation of fibers on the pullout behavior of reinforcement bar embedded in ultra high performance concrete, *Construct Building Mater* 146 (2017) 582–593.
- [37] M. Roy, Development and Evaluation of High Performance Fiber Reinforced Concrete as a Repairing Material. Master's Thesis, West Virginia University, 2011.
- [38] M. Roy, I. Ray, J.F. Davalos, High-performance fiber-reinforced concrete: Development and evaluation as a repairing material, *J Mater Civ Eng* 26 (10) (2014) 04014074.
- [39] G. Ruano, F. Isla, D. Sfer, B. Luccioni, Numerical modeling of reinforced concrete beams repaired and strengthened with SFRC, *Eng Struct* 86 (2015) 168–181.
- [40] M. Safdar, T. Matsumoto, K. Kakuma, Flexural behavior of reinforced concrete beams repaired with ultra-high performance fiber reinforced concrete (UHPFRC), *Compos Struct* 157 (2016) 448–460.
- [41] H.P. Schwefel, Evolutionsstrategie und numerische Optimierung, Dissertation, Technische Universität Berlin (1975).
- [42] G.N. Smith, Probability and statistics in civil engineering, Collins, London, 1986.
- [43] S. Soleimani, P. Jiao, S. Rajaei, R. Forsati, A new approach for prediction of collapse settlement of sandy gravel soils, *Eng Comput* 34 (1) (2018) 15–24.
- [44] S. Soleimani, S. Rajaei, P. Jiao, A. Sabz, Soheilinia, New prediction models for unconfined compressive strength of geopolymer stabilized soil using multi-gene genetic programming, *Meas* 113 (2018) 99–107.
- [45] B.A. Tayeh, B.H.A. Bakar, M.A.M. Johari, Characterization of the interfacial bond between old concrete substrate and ultra high performance fiber concrete repair composite, *Mater Struct* 46 (2013) 743–753.
- [46] N.T. Tran, T.K. Tran, J.K. Jeon, J.K. Park, D.J. Kim, Fracture energy of ultra-high-performance fiber-reinforced concrete at high strain rates, *Cement Concrete Res* 79 (2016) 169–184.
- [47] M. Unal, M. Onat, M. Demetgul, H. Kucuk, Fault diagnosis of rolling bearings using a genetic algorithm optimized neural network, *Meas* 58 (2014) 187–196.
- [48] T. Weise, *Global Optimization Algorithms—Theory and Application*. Germany: it-weise.de (self-published), 2009. Available at: <http://www.it-weise.de>.
- [49] J. Xia, T. Chan, K.R. Mackie, M.A. Saleem, A. Mirmiran, Sectional analysis for design of ultra-high performance fiber reinforced concrete beams with passive reinforcement, *Eng Struct* 160 (2018) 121–132.
- [50] F. Yan, Z. Lin, X. Wang, F. Azarmi, K. Sobolev, Evaluation and prediction of bond strength of GFRP-bar reinforced concrete using artificial neural network optimized with genetic algorithm, *Compos Struct* 161 (2017) 441–452.
- [51] D.Y. Yoo, S.T. Kang, N. Banthia, Y.S. Yoon, Nonlinear finite element analysis of ultra-high-performance fiber-reinforced concrete beams, *Int J Damage Mech* 26 (5) (2017) 735–757.
- [52] D.Y. Yoo, H.O. Shin, J.M. Yang, Y.S. Yoon, Material and bond properties of ultra high performance fiber reinforced concrete with micro steel fibers, *Compos B* 58 (2014) 122–133.
- [53] C. Zang, M. Imregun, Structural damage detection using artificial neural networks and measured FRF data reduced via principal component projection, *J Sound Vib* 242 (5) (2001) 813–827.
- [54] B. Zhou, Y. Uchida, Relationship between fiber orientation/distribution and post-cracking behavior in ultra-high-performance fiber-reinforced concrete, *Cement Concrete Compos* 83 (2017) 66–75.
- [55] Q. Zhou, F. Zhu, X. Yang, F. Wang, B. Chi, Z. Zhang, Shear capacity estimation of fully grouted reinforced concrete masonry walls using neural network and adaptive neuro-fuzzy inference system models, *Construct Build Mater* 153 (2017) 937.